Subwavelength direct laser nanopatterning via microparticle arrays for functionalizing metallic surfaces

Romano, Jean-Michel; Ahmed, Rajib; Garcia Giron, Antonio; Penchev, Pavel; Butt, Haider; Dellea, Olivier; Sikosana, Melissa; Helbig, Ralf; Werner, Carsten; Dimov, Stefan

DOI:
10.1115/1.4042964

Document Version
Peer reviewed version

Citation for published version (Harvard):
Romano, J-M, Ahmed, R, Garcia Giron, A, Penchev, P, Butt, H, Dellea, O, Sikosana, M, Helbig, R, Werner, C & Dimov, S 2019, 'Subwavelength direct laser nanopatterning via microparticle arrays for functionalizing metallic surfaces', *Journal of Micro and Nano-Manufacturing*, vol. 7, no. 1, 010901. https://doi.org/10.1115/1.4042964

Subwavelength Direct Laser Nanopatterning via Microparticle Arrays for Functionalizing Metallic Surfaces

Jean-Michel Romano[1]
University of Birmingham
School of Engineering, University of Birmingham, Edgbaston, Birmingham B15 2TT, United Kingdom
J.Romano@bham.ac.uk

Rajib Ahmed
Stanford University
Bio-Acoustic MEMS in Medicine (BAMM) Laboratory, School of Medicine, Stanford University, Palo Alto, CA 94304, USA
&
University of Birmingham
School of Engineering, University of Birmingham, Edgbaston, Birmingham B15 2TT, United Kingdom
rajibah@stanford.edu

Antonio Garcia-Giron
University of Birmingham
School of Engineering, University of Birmingham, Edgbaston, Birmingham B15 2TT, United Kingdom
A.GarciaGiron@bham.ac.uk

Pavel Penchev
University of Birmingham
School of Engineering, University of Birmingham, Edgbaston, Birmingham B15 2TT, United Kingdom
P.Penchev@bham.ac.uk

Haider Butt
University of Birmingham
School of Engineering, University of Birmingham, Edgbaston, Birmingham B15 2TT, United Kingdom
H.Butt@bham.ac.uk

[1] Corresponding Author: Jean-Michel Romano (jean-michel.romano@gadz.org)

Olivier Delléa
CEA
L2CE, Laboratoire des Composants pour le Conversion de l'Energie, CEA/LITEN, Laboratoire d'Innovation pour les Technologies des Energies Nouvelles et des nanomatériaux, Grenoble, France
olivier.dellea@cea.fr

Melissa Sikosana
Leibnitz IPF
Max Bergmann Center of Biomaterials, Leibniz Institute of Polymer Research Dresden, 01069 Dresden, Germany
sikosana@ipfdd.de

Ralf Helbig
Leibnitz IPF
Max Bergmann Center of Biomaterials, Leibniz Institute of Polymer Research Dresden, 01069 Dresden, Germany
helbig@ipfdd.de

Carsten Werner
Leibnitz IPF
Max Bergmann Center of Biomaterials, Leibniz Institute of Polymer Research Dresden, 01069 Dresden, Germany
werner@ipfdd.de

Stefan Dimov
University of Birmingham
School of Engineering, University of Birmingham, Edgbaston, Birmingham B15 2TT, United Kingdom
S.S.Dimov@bham.ac.uk

ABSTRACT

Functionalized metallic nano-features can be selectively fabricated via ultrashort laser processing, however the cost-effective large-area texturing, intrinsically constrained by the diffraction limit of light, remains a challenging issue. A high-intensity near-field phenomenon that takes place when irradiating micro-sized spheres, referred to as Photonic Nanojet (PN), was investigated in the transitional state between geometrical optics and dipole regime to fabricate functionalized metallic subwavelength-features. Finite element simulations were performed to predict the PN focal length and beam spot size, and nano-feature formation. A systematic approach was employed to functionalize metallic surface by varying the pulse energy, focal offset and number of pulses to fabricate controlled array of nanoholes and to study the generation of triangular and rhombic Laser-Induced Periodic Surface Structures (LIPSS). Finally, large-area texturing was investigated to minimize the dry laser cleaning effect and improve homogeneity of PN-assisted texturing. Tailored dimensions and densities of achievable surface patterns could provide hexagonal light scattering and selective optical reflectance for a specific light wavelength. Surfaces exhibited controlled wetting properties with either hydrophilicity or hydrophobicity. No correlation was found between wetting and microbacterial colonization properties of textured metallic surfaces after 4h incubation of E. coli. However, an unexpected bacterial repellency was observed.

1. INTRODUCTION

Techniques for selective micro- and nanopatterning of metallic surfaces have attracted a growing interest due to their novel optical [1–3], wettability [4–6], and anti-microbiological [7–11] applications. Several non-lithographic techniques were suggested to fabricate subwavelength-size patterns, such as single and multi-beam direct laser interference patterning [12,13] or polarization-based laser-induced periodic surface structures (LIPSS) [14]. In the last 10 years, a promising nanofabrication route involving microparticles as near field focal enhancement systems was developed [15,16]. This method benefits from the near field optical phenomena, called Photonic Nanojet (PN), that allows a beam focusing beyond the optical diffraction limit of light [17–19]. However, a preliminary step is required to apply the PN technology for surface texturing, i.e. the deposition of a microspheres' monolayer on a substrate. Self-assembly processes such as Langmuir-Blodgett techniques can be applied for microspheres' deposition into hexagonal close-packed (HCP) monolayers, also called contacting particle-lens arrays (CPLA) [20]. Then, a laser-irradiation of CPLA results in an array of non-evanescent beams emerging from the shadow-side of microspheres, with diameters as small as the third of the irradiated wavelength and a length of two wavelengths [15]. Such a method was applied to laser-fabricate subwavelength holes and convex bumps [21,22], even on materials with low absorption at a given wavelength (λ) [23,24]. Various attempts to tailor the PN optical properties were reported, including changing the refractive index (n) and the shape and diameter (2r) of microspheres and also the illumination conditions [15,25–28].

However, large-area texturing for functionalizing surfaces by direct laser ablation remains a challenge. This is mostly due to the detachment of microspheres after any single laser pulse irradiation and this could be explained with the substrate ablation or dry laser cleaning (DLC) effect [29–32]. Contrary to laser cleaning where the laser-induced marking is an undesirable side-effect, to achieve large-area PN texturing the marking must be maximized while minimizing the microspheres' detachment. Several techniques were proposed to address this issue, usually by preserving CPLA by covering it with a transparent material [33–36]. Maintaining CPLA in contact with the substrate allowed multi-pulse processing and thus to texture larger areas homogeneously and at the same time to increase the aspect ratio of the resulting nanoholes [36].

In this research, a novel approach for submicron large-area texturing of metallic surfaces is presented and their multifunctional aspects are described with applications in nano-scale optics, wettability and microbiology. Especially, a near-infrared ultrashort laser irradiation of transparent silica microspheres deposited onto stainless steel plates was investigated. The microspheres were used as CPLA and their sizes were equal to the irradiation wavelength. FE simulations were conducted to predict the PN focal length and the full width at half maximum (FWHM) spot size at the substrate surface while varying laser wavelengths and spheres' radii. Direct laser nanofabrication of nanobumps, nanoholes and LIPSS was investigated and was compared to DLC effect towards large-area texturing. Finally, potential surface functionalities of nanoholes and LIPSS were studied for selective hexagonal scattering, tunable optical reflection, wettability, and microbiology applications.

2. MATERIAL AND METHODS

2.1. Sample preparation and laser set-up

Silica microspheres were deposited in a hexagonal close-packed monolayer onto X6Cr17 stainless steel plates by employing a patented method [37] based on the Langmuir-Blodgett technique. The laser irradiation was performed with a near-infrared ultrashort pulsed laser source (Satsuma, Amplitude Systemes) with a pulse length of 310fs and a central wavelength of 1032nm. The laser beam had a circular polarization and was steered over the substrate using a 3D scan head (RhoThor RTA) equipped with a 100mm F-theta telecentric lens. The beam spot size, $2\omega_0$ at $1/e^2$, was adjusted to 30µm diameter at the focal point with a beam expander. Spot sizes at focal offset were calculated following the relation $\omega(z)=\omega_0[1+(z/Z_R)^2]^{1/2}$ with $Z_R=\pi\omega_0^2/\lambda$. Pulse fluences were estimated by dividing the pulse energy by the spot area $\pi\omega^2$. For post-fabrication of LIPSS, the pulse-to-pulse distance (δ) is the ratio of the scanning speed over the repetition rate and the number of pulse equivalent was calculated according to the formula $N=\pi\omega_0^2/(\sigma\cdot\delta)$, with σ the hatching distance. The remaining spheres and any debris resulting from the laser irradiation were removed using an ultrasonic bath in ethanol for 15min.

2.2. Microscopic imaging

The SEM micrographs were produced using a scanning electron microscope (Hitachi TEM3030Plus) with secondary electron detector and low vacuum. Fourier transforms (2D-FFT) of the images were performed in Gwyddion imaging tool. In

addition, the 3D topographies were measured using an atomic force microscope (AFM, Dimension 3100, Bruker) equipped with AFM probes (PPP-RT-NCHR, Nanosensors) in tapping-mode.

2.3. Optical characterization

A broadband light source (400-1100nm, Ocean Optics 2000+) and a spectrophotometer (resolution 0.1-100 FWHM, Ocean Optics HL 2000) were used to characterize the surfaces' optical properties. Broadband light normally illuminated the metallic nanopatterns and the reflected light was captured though an objective (x20) in reflection mode. Near-field hexagonal scattered/diffracted light was measured through a hemispherical screen (semi-transparent white, 30mm in diameter). Far-field scattered/diffracted rainbow patterns were performed with an image screen (white A4 paper) setup.

2.4. Wettability

The wetting properties were analyzed employing an optical tensiometer (Attension Biolin Scientific Theta T2000-Basic+) and purified (Milli-Q, Merck) water was used as probe liquid. All tests were performed under ambient conditions. Static contact angles (CA) of 6µl drops were measured after stabilization employing the sessile drop technique. The CA hysteresis was calculated using the needle-in-drop method and measuring the advancing and receding CA evolution of 6µl at 0.5µl/s.

2.5. Microbiology

The textured metallic samples were replicated by a two-step process. First, negative surface structures were obtained from a master with an epoxy resin (Araldit CY212, Plano) via thermal polymerization. Second, the final replicas were produced by employing the epoxy resin master with a perfluoropolyether prepolymer via UV induced polymerization (Fluorolink MD40, Solvay). Bacterial colonization and bacterial adhesion on textured substrates were assessed with E. coli (strain W3110), after 4h incubation in lysogeny broth media (LB, Sigma-Aldrich) at 37°C (overnight culture adjusted to optical density (OD) ~0.4 in fresh LB before). The bacteria were fixed in paraformaldehyde (PFA), then rinsed with phosphate buffer solution and distilled water (milliQ, Merck) and gently dried with nitrogen. Subsequently, the samples were sputter coated with a 10nm gold layer (SCD 050 sputter coater, Balzers) and imaged with a SEM XL30 (ESEM/FEG, FEI). The adherent bacterial cells were counted on SEM images using the cell counter tool in ImageJ (NIH). The experiment was performed two times and a total of 14 images (~150000μm^2) per sample were examined.

3. RESULTS AND DISCUSSION

3.1. FE and computational modelling

Computational modelling techniques for particle light scattering were developed, in particular by employing numerical simulation or analytical methods based on the generalized Lorentz-Mie theory [26,30]. Such techniques were often applied for

particles with much larger sizes than the wavelength and the focal spot sizes were calculated to be in the range from 0.8λ down to 0.15λ depending on the refraction indexes of the particles and the propagation medium [21,38,39]. Depending on the ratio $2r/\lambda$ (x) three different cases could be distinguished. For x>>1, the generic rules of geometrical optics apply and the Snell-Descartes' law should be used to obtain the approximate focal spot size (w_g) as follows [30]:

$$w_g \approx r((4-n^2)^3/(27n^4))^{1/2} \quad (1)$$

For spheres much smaller than the wavelength, x<<1, the close-packed monolayer behaves as a densely homogenous one and the dipole approximation estimated the spot sizes (w_d) in the dipole regime similar to the sphere radii [30], i.e. $w_d \approx r$, which is comparable with some reported simulation results [40]. Seldom, the intermediary range between geometrical and dipole regime, i.e. x≈1, was considered and so the focal spot size could be estimated between 0.14λ and 0.40λ [39,41,42]. For this third case, Arnold [30] introduced a constant of transition $C=((n^2-1)w_g)/((n^2+1)r)$ thus unifying the analytical approximation of geometrical and dipole focal enhancement so that the focal spot size (w) could be approximated as follows:

$$w=(w_d+Ck^2r^2w_g)/(1+Ck^2r^2) \quad (2)$$

where $k=2\pi/\lambda$ is the electromagnetic wave number.

To understand the near-field focal enhancement via microspheres, FE based computational modelling was performed in COMSOL Multiphysics (v5.3a). A planar wave (1030nm) propagates through an air medium and focused through silica microspheres. To take into account optical interferences of the spheres, a close-packed

2D array of 5 spheres was considered. The continuity and scattering boundary conditions were considered for the spheres and the domain boundaries. The diameter 2r of the microspheres was varied, and respectively, the domain of simulation (8r x 10r). Near-field electric field intensity distributions upon normal irradiation of microspheres of different sizes were investigated by varying x from 0.5 to 8. The microspheres are considered as a homogeneous, non-absorbent medium with refractive index of 1.50 at 1030nm wavelength [43]. The near-field focused light intensity as a function of microsphere size (x=1.0, 1.9, and 2.9) are depicted in Figure 1a. The increase of microspheres sizes of led to an increase of the focused light (D) and PN length (L). For periodic microsphere arrays, the maximum focused light intensity was observed at the center due to the Gaussian distribution nature of the illuminated plane wave.

The resulting PN was analyzed by means of peak intensity (I_{max}), paraxial focal length (D) and beam spot size (FWHM at I_{max}). The PN length (L) was estimated as the distance from the substrate surface until the intensity reaches $I_{max}/2$ as shown in Figure 1a, by plotting the evolution of intensity along the vertical axis (Figure 1b). The intensity and beam spot size at the point of contact between the microspheres and the substrate was considered, too. Figure 1c showed peak intensity of PN as a function of normalized microsphere size at maximum and surface position. A pre-condition for the near field optical phenomena associated with PN is the electric field propagation along the vertical axis to reach a peak intensity outside the microsphere. Based on the simulation results this pre-condition is met at x≈1.5 and x larger than 2 (see Figure 1d). Therefore, the PN geometrical optic regime is considered established for x strictly larger than 2. For this

regime, the relative peak intensity increased with the size of the sphere (see Figures 1c-d). However, while the peak intensity is reached at the substrate surface when x=2, a further increase of x led to a reduction of the surface peak intensity compared with the max values, especially up to approximately 50% for x>6. Another well-established PN trend depicted in Figure 1d is that both the focal point and the PN length decrease with the decrease of microspheres' sizes [19,44] until the focal point becomes coincident with the contact point between the microspheres and the substrate for x=2. Interestingly, the simulation illustrated that a further decrease of x led to an increase of the focal distance, when x=1.5, before a rapid decrease down to negative values where the peak intensity was reached inside the microspheres. This was attributed to a transition state between the geometrical optic and dipole regimes. For the dipole regime (x<<1), electrical fields are predicted to reach a peak intensity not anymore along the vertical axis but sideways [40]. The FE simulation exhibited local intensity peaks shifted sidelong the paraxial axis for the transition state of x≈1 and the focal point is close to the microsphere's center. Half maximum intensity was reached outside the microsphere, at a paraxial distance of ~0.2λ, which is considered as a PN tail. Furthermore, considering characteristics of Gaussian intensity profiles, the PN tail reached an intensity of I_{max}/e^2 at a paraxial distance of approximately 0.7λ for x≈1. Even if the peak intensity is not reached on the substrate, the intensity at the surface may still exceed the ablation threshold for a given material, opening the way for PN-assisted manufacturing applications.

A subwavelength-size damage may appear on substrate surface when the PN energy density is sufficiently high while the PN beam size is smaller than the irradiating wavelength. The analytical approximation for the focal spot size in Eq. (2) converted to FWHM by a factor of $(2\ln 2)^{1/2}$ correlated well to the simulation of PN beam size for x lower than 1.5, with FWHM smaller than 0.5λ. Although the analytical model predicts a constant increase of beam size with the increase of x, the FWHM reached a plateau at around 0.5λ in the FE simulation, in particular for x larger than 1.5 (see Figure 1e). A similar stagnation was also reported by McCloskey et al. [26]. While the PN FWHM appeared consistently in the subwalength range, with a minimum at ~0.2λ, the FWHM at the surface position remained in the subwavelength range only for x from 0.5 to 4. Therefore, when PN are used in direct contact with substrates, two fabrication regimes can be discussed. At first regime, an increase of microspheres' sizes inherently leads to larger surface beam sizes and hence a lower intensity at the surface. This effect may be comparable to performing laser processing out of focus, but only to some extent, as any change in the PN beam shape may induce different surface damage morphologies. The simulation results' trend for microspheres much larger than the wavelength used in contact mode may confirm experimental observation of volcano-shaped surface damages [22,45]. Several studies investigated how to bring the focal point back to the surface, with a vertical offset of the microspheres [42,46,47] or a non-orthogonal incident irradiation [40,48,49], and this aspect is therefore not considered further in this study. At second regime, the irradiation of particles smaller than the wavelength leads to FWHM at the surface position that are in the subwalength range, but with the lowest

peak intensity and PN length. Thus, this constrains the fabrication process to low aspect ratio nanofeatures and therefore should be investigated further.

Employing CPLA for large area texturing, the HCP nature of the deposited monolayer induces a surface damage with hexagonal periodicity equal to the microspheres' size. However, the dimension of the surface damages compared to their periodicity has to be considered. The irradiation density, i.e. the ratio of the area covered by PN spots with intensity larger than half maximum over the whole substrate, can be used as an indicator for the achievable feature sizes and periodicity (Figure 1f). A general trend between the analytical and simulation results was observed, the irradiation density increasing with the decrease of x. The analytical approach predicts an asymptotic minimum at ~2% for very large x and a maximum irradiation density of ~30% can be achieved as x tends to 0. Contrarily, the simulations revealed a local maximum of ~20%, reached when x is equal to 1. There are similar trends in approximation and simulation results but there are discrepancies, too, because the analytical approach does not take into account whether the beam spot sizes are at the substrate surface or not. For PN spots on the surface, the density is also increasing for lower x. The ratio FWHM/2r reached more than 50% when 2r is smaller than λ, indicating that the density achievable with the PN technology can be sufficient for large-area sub-wavelength surface texturing when using CPLA with microspheres smaller than the wavelength.

In this research the case when x is equal to 1 is selected to investigate the PN texturing process experimentally. Especially, this PN processing case is used to validate the technology for producing dense nanoscale features while the irradiation conditions

are far from optimum. In particular, these PN texturing conditions lead to the lowest peak intensity and intensity at the surface (Figure 1c), and a PN tail of a few hundred nanometers (Figure 1d), however with a relatively high irradiation density with subwavelength-sized FWHM in a λ-periodic HCP (Figure 1f).

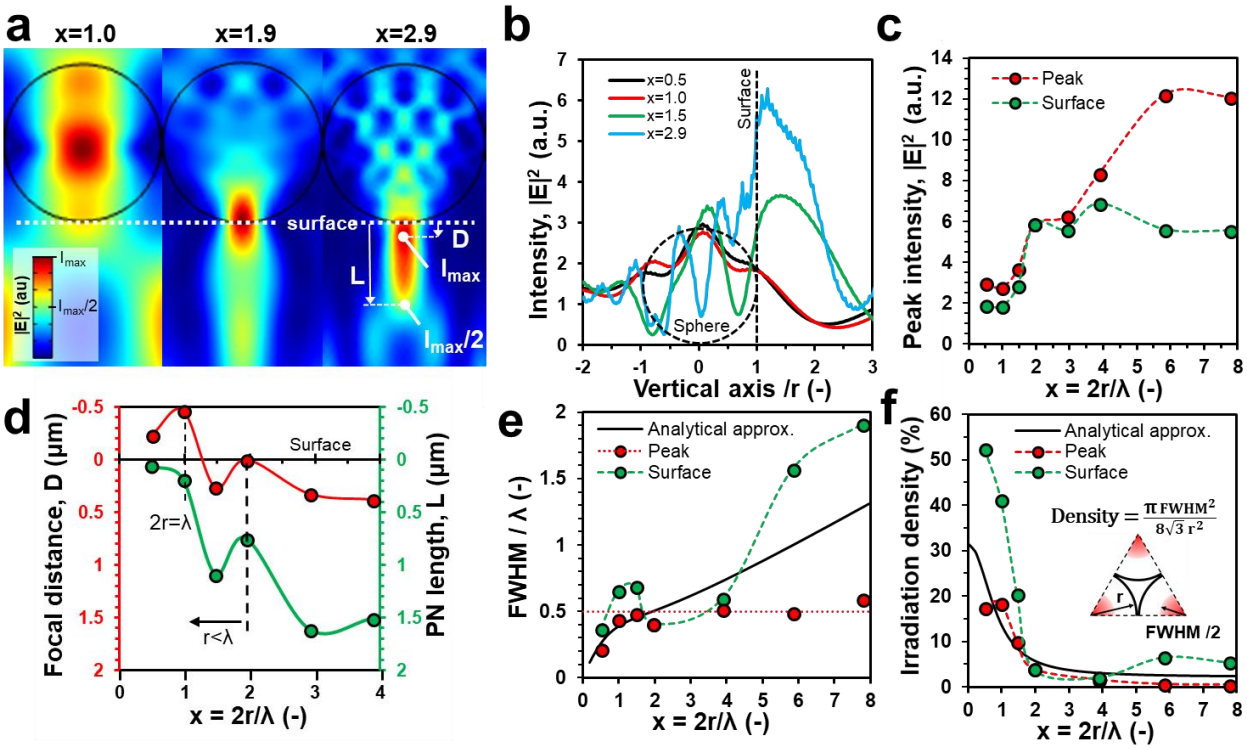

Figure 1. The modelling results of light focusing through silica microspheres. Irradiation wavelength was fixed at 1030nm while the microspheres' radii were varied. (a) Intensity mapping for three cases of x=2r/λ, especially equal to 1.0, 1.9 and 2.9. The color scales are independent for each case, in particular from blue (low intensity) to red (peak intensity). (b) The intensity evolution along the vertical axis, normalized with the sphere's radius for four cases of x. The dashed circle and line indicate the normalized sphere's dimension and surface position. (c) Peak intensity estimations for the considered cases of x from 0.5 to 8. (d) Paraxial focal length and PN length as a function of x. The red colored area suggests combinations of wavelength and radius where the focal point is outside microspheres. (e) FWHM normalized in regard to the irradiation wavelength for the considered x values. (f) Irradiation surface density calculated for a close-packed array of spheres as a function of x. Estimations are taken at the peak intensity positions z=z(I_{max}) on the substrate surface. Analytical PN waist were plotted according to Arnold [30].

3.2. PN-assisted surface texturing

3.2.1 Subwavelength laser ablation

Ultra-short laser pulses in the near-infrared (NI) range (310fs, 1032nm) were used to irradiate a dense monolayer of 1µm-diameter SiO2 spheres deposited onto stainless steel substrates (Figure 2a). The laser beam was steered over the surface using a galvanometer scanner and was focused with a 100mm F-θ-lens. The NI irradiation with a 30µm beam spot creates an array of PN tails that can lead to surface damage when the pulse energy is sufficiently high, resulting in the ejection of parts of the CPLA (Figures 2b-c). Each PN resulting from such CPLA irradiation can be considered as a Gaussian nanobeam, with FWHM and $1/e^2$ spot sizes of 0.46λ and 0.74λ, respectively. Various surface morphologies could be achieved depending on pulse energy and pulse numbers. A selection of PN-processed surfaces is presented in Figures 2d-g. As a result of a repeated irradiation with a pulse energy close to the damage threshold, convex nanobumps were fabricated (Figure 2d). Huang et al. attributed the generation of such surface features to the Marangoni convection induced by PN sidelong the paraxial axis and achieved λ/2-diameter nanobumps on silicon wafers by irradiating a 1-µm-diameter CPLA with UV-nanosecond laser pulses [50]. In this research, slightly smaller nanobumps, in particular with diameters and heights of ~λ/3 and ~30nm, respectively, were generated with near-infrared (NI) 310fs pulses. While a single shot was sufficient to create the nanobumps with nanosecond pulses, multiple irradiations, in particular 100 pulses at 10kHz, were required to produce them with femtosecond pulses, and apparently as a result of some cumulative effects.

Beyond the damage threshold of the substrate, the surface was locally ablated under the microspheres and an array of nanoholes were generated. First, a surface damage was observed with single pulses of 0.9μJ at the focal point and then up to 1mm focal offset. The nanoholes were circular in shape with a distance between each other corresponding to CPLA periodicity. The minimum diameter was ~λ/6, i.e. ~175nm. The increase of pulse energy resulted in larger holes' diameters, up to 1μm, and thus to form honeycomb structures. For positive or negative surface structures, the aspect ratio remained limited at ~1:10, as depicted by two representative AFM cross-sections in Figures 2k-l. The microspheres' sizes were close to the irradiation wavelength (x≈1) in this research and these processing conditions differ from those used by other researchers for direct NI femtosecond nanopatterning. In particular, wavelengths in the range from 400 to 800nm were utilized to fabricate nanoholes of ~0.3λ diameter and several 10nm in depth on silicon and glass substrates [40,51].

The intensity distribution of the laser beam had a direct influence on the homogeneity of fabricated nanoholes' arrays. A single pulse could produce an array of ~260 nanoholes with diameters from 255 to 940nm (Figure 2h). An increase of pulse energy results in ~730 nanoholes with similar average diameter but with a broader dispersion, from 120nm to 1.23μm (Figure 2i). Such high pulse energies were detrimental to the nanoholes' homogeneity and this was mostly due to the laser beam Gaussian intensity profile. PN induced thermal-effects after irradiations with femtosecond laser pulses were reported on glass [51], silicon wafers [45,52] and metallic substrates [52]. Especially, they led to the fabrication of nanoholes larger than

the CPLA periodicity and thus clogging contiguous nanoholes. However, by tailoring the focal offset, larger CPLA areas could be irradiated and also the use of laser beams with a top-head Gaussian profiles could enable the fabrication of nanoholes with much smaller spread of diameters. In this work, arrays of nanoholes were produced with a focal offset up to 2mm. Especially, it was possible with the use of 1mm focal offset to produce ~1700 nanoholes with an average diameter 310nm and a spread from 160 to 780nm (Figure 2j).

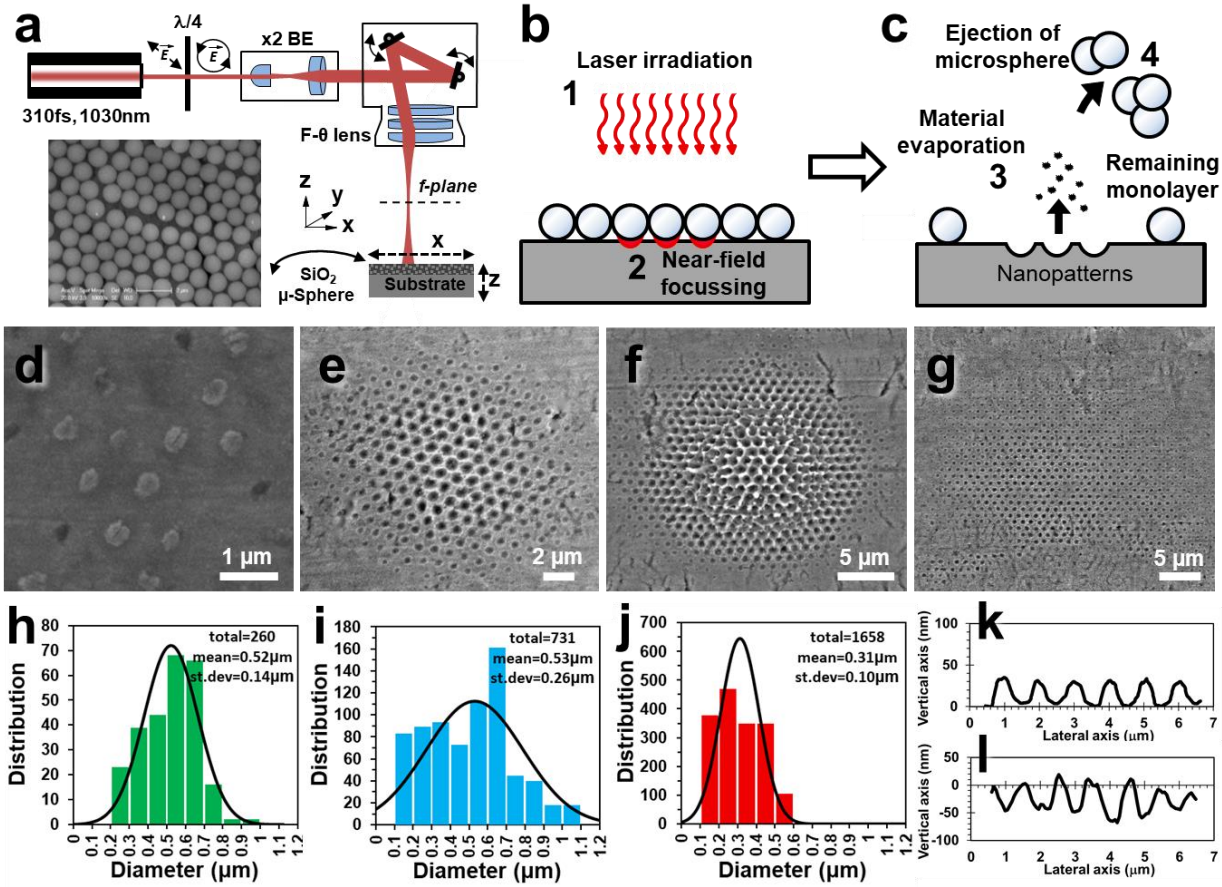

Figure 2. A direct laser ablation based nanopattering by irradiating a HCP CPLA of 1μm-diameter spheres with a NI 30μm-diameter Gaussian fs-laser beam. (a) The used experimental setup for processing substrates with a focal offset. (b-c) The schematic steps of the texturing process. The microspheres are partially removed from the textured area and its surroundings. Micrographs of morphologies achieved with 310fs laser pulses at 1032nm wavelength: (d) nanobumps fabricated employing a 2mm focal

offset and 100 irradiations at 1.3μJ; array of nanoholes fabricated with a single irradiation of (e) 1.3μJ at focus, (f) 6.3μJ at focus and (g) 6.3μJ at 1mm focal offset, respectively. (h-j) Distributions of nanoholes' diameters corresponding to (e-g). The nanoholes are gathered in clusters of 0.1μm and a normal distribution is extrapolated from the distribution. Profiles of nanobumps (k) and honeycomb structures (i) are given with two representative AFM cross sections.

3.2.2 Large area texturing

Parallel nanostructuring refers to the fabrication of nanofeatures over an area significantly bigger than a single-pulse laser spot. The large area covering with PN-induced nanofeatures is intrinsically limited due to the detachment of microspheres after any single laser pulse irradiation. This is similar to the effect referred to as Direct Laser Cleaning (DLC) that was investigated by many researchers both empirically [31] and theoretically [30]. Especially, DLC is the result of a mechanical ejection triggered by the rapid thermal expansion of the irradiated microspheres. The evaporation of condensed humidity at the interface sphere-substrate may also increase DLC effect [32].

DLC takes place below the ablation threshold and therefore only cracks and delamination of the CPLA could occur without any surface damage, until a sufficient fluence is reached to eject the microspheres. The reported ejection velocities [53] are in the order of 10m/s and this could explain why there was no increase of nanoholes' aspect ratios with the pulse repetition rates investigated in this research. A pulse energy of 2μJ and processing with 1.5mm focal offset were required to start cracking the microspheres' monolayer. A further increase of pulse energy up to 4.8μJ resulted in a partial removal of microspheres without damaging the substrate surface. At the same time laser processing closer to the focal point and also with higher pulse energies led

inevitably to surface damage. The CPLA delamination and ejection of microspheres can be attributed to ablation dynamics, especially the removal of microspheres above nanotextured areas.

A focal offset of the incident laser beam was beneficial for fabricating more homogeneous array of nanoholes, however the tail of the Gaussian beam broadens the area affected by DLC. A multi-pulse approach had the same DLC effect, possibly due to a cumulative effect. Similarly, a higher pulse energy increased not only the thermal effect and nanoholes' sizes but also the DLC area as shown in Figure 3a. The filling ratio, in particular the ratio between the surface area covered with nanofeatures and the total processed area, was optimized by applying various scanning strategies, especially by varying the pulse-to-pulse distance to achieve moon-shaped arrays of nanoholes, as shown in Figure 3b. For example, the maximum filling ratio of 46% was reached with 3.6μJ pulses at focus and a pulse-to-pulse distance slightly smaller than the laser spot diameter (Figure 3c). A further reduction of pulse-to-pulse distance led to non-circular arrays of nanoholes and decreased the filling ratio to ~30% (Figures 3d-e) until the LIPSS outset threshold was reached and PN-induced nanoholes were converted into ripples-like LIPSS (Figures 3f-g).

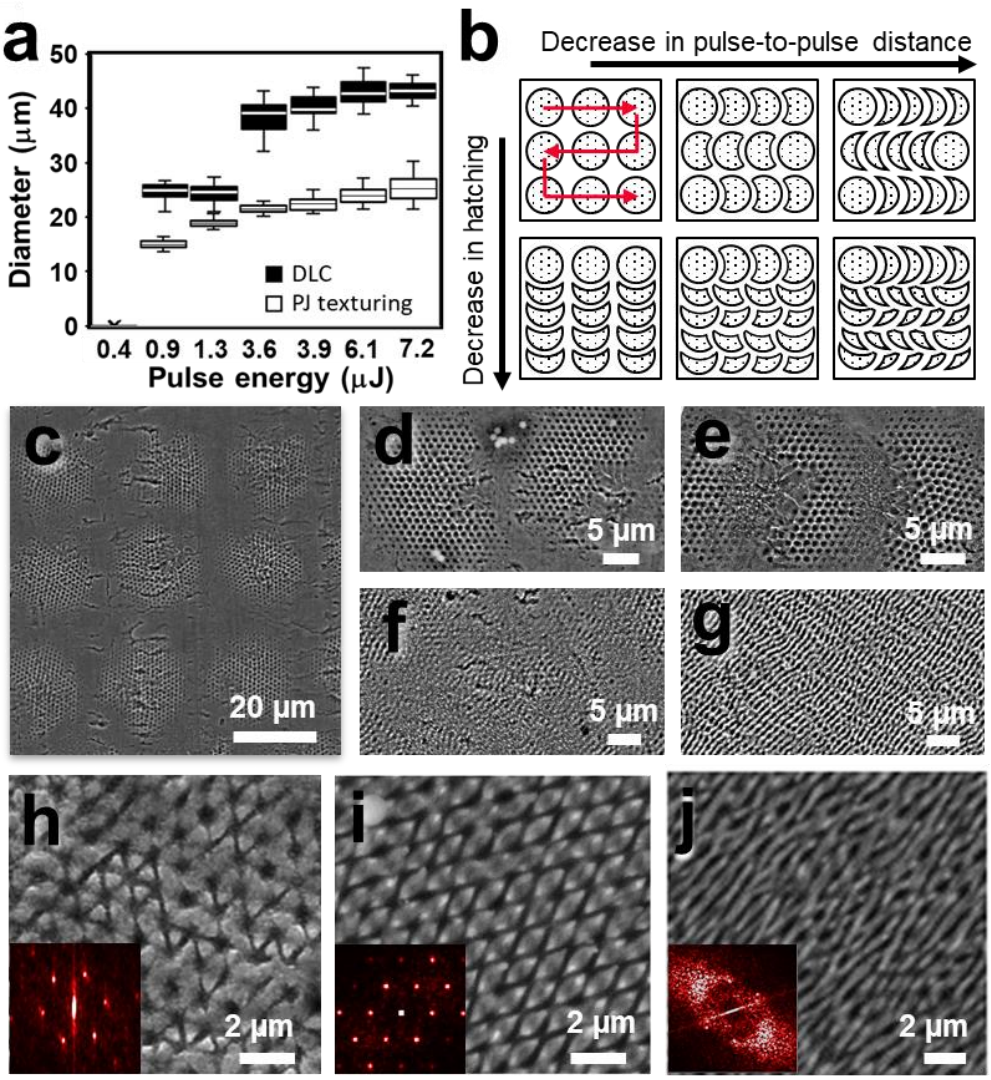

Figure 3. A large area texturing with nanoholes after near-infrared irradiation (λ=1032nm, circular polarization, 30μm focal spot size) of a CPLA of 1-μm-spheres. (a) The diameters of DLC spots compared with the diameter of those covered with PJ-induced holes, as a function of pulse energy at focus. Mean diameters and their standard deviation were calculated based on 5 measurements. (b) Schematic representation of textured areas that result from varying hatching and pulse-to-pulse distances, σ and δ, respectively. Micrographs depict the effects on surface morphologies when varying σ and δ, in particular: (c) σ=δ=25μm, (d) δ=22.5μm and σ=25μm, (e) δ=15μm and σ=25μm, (f) σ=δ=10μm and (g) σ=δ=5μm, with 3.6μJ pulses at focus. LIPSS generation upon multiple irradiations of pre-fabricated arrays of nanoholes: (h) hexagonal LIPSS fabricated at 1mm focal offset by 100 2.5μJ pulses. Further evolution of LIPSS over nanoholes fabricated with 3.9μJ pulses at focus: (i) rhombic-shaped LIPSS after 28 0.5μJ pulses at focus and (j) ripples-like LIPSS after 177 1.5μJ pulses at focus.

The Fourier transformed micrographs indicating LIPSS periodicity and orientation are depicted in the insets.

3.2.3 LIPSS generation with tailored periodicity

Further irradiation of nanoholes fabricated with single-pulses with fluences in the range from 0.18 to 0.29J/cm^2, as shown in Figure 2g, did not lead to additional material removal but resulted in some improvements of nanoholes' rims, as already reported [24,54]. The irradiation intensity was sufficient to displace the microspheres from their initial locations and thus to prevent the fabrication of nanoholes with higher aspect ratio unless preventing such displacements [36]. Albeit the fluences used for nanoholes' fabrication were not sufficient to reach the substrate's ablation threshold after the CPLA removal, multiple irradiations led to surface structures referred to as LIPSS [14]. Cumulative fluence of ~1.8J/cm^2 was sufficient to trigger the generation of LIPSS over the arrays of nanoholes. Further cumulative effects after reaching ~2.9J/cm^2 were the spreading of LIPSS over the whole surface and thus to join the array of nanoholes. At a fluence of ~11J/cm2 the formation of triangular surface morphologies was initiated (Figure 3h) and, compared with the generation of such triangular LIPSS without CPLA, only half of the necessary cumulative fluence was required [6]. Thus, pre-fabricated surface patterns could be used to lower the cumulative fluence required for LIPSS generation.

Despite LIPSS being wavelength-dependent periodic surface structures, the 1µm periodicity of the CPLA was retained. Various regular LIPSS morphologies were generated by varying pulse numbers and fluence, in particular triangular and rhombic

LIPSS (Figures 3h-i), which could be of interest for a single-step LIPSS fabrication. The periodicity remained consistent with the pre-fabricated array of nanoholes until the cumulative fluence was sufficient to break down the established λ-periodic triangular features into ~0.82λ-periodic ripple-like LIPSS (Figure 3j). Considering the case in Figure 3h (λ periodic), such triangular LIPSS with ~0.87λ periodicity were achieved with similar irradiation conditions where the triangular surface morphology was attributed to the use of a circular-polarized laser beam [6]. A pre-fabricated array of nanoholes can potentially enable the generation of triangular nanofeatures with varying sizes and periodicity.

3.3. Surface functionalization

3.3.1 Optical properties

The sub-wavelength features fabricated on stainless steel were characterized through light illumination in reflection mode. A broadband light source was used to illuminate the textured surfaces at angles from 0 to 180° by controlling the rotation with a step motor. A spectrophotometer was positioned normal to the patterned surface for intensity measurements within the visible spectrum, i.e. a wavelength range from 400 to 700nm.

The optical response of stainless steel surfaces fabricated with different pulse energies, pulse numbers and effective pulse-to-pulse distances were studied. A 0.9μJ-single pulse irradiation resulted in a surface morphology with reflection properties close to 100% with only a slight decrease to around 85% in the violet-blue range (Figure 4a).

Higher pulse energies led to a decrease of the overall reflection spectrum as a result of the high filling ratio (Figure 4b). In single pulse processing, the reflection properties could be finely tailored in the range from 100 to 80% by varying the pulse energy from 0.9 to 6.6μJ. An increase in pulse numbers led to an overall decrease of reflection properties that can be attributed to the respective progressing changes in LIPSS morphologies (Figures 4a-b). Overall, the reflection of wavelengths in the violet-blue range was lower compared to green and red lights (Figure 4c).

A decrease of pulse-to-pulse distance while keeping the hatch distance the same led to a decrease of overall reflection spectrum except for the red light that remained unchanged. Similarly, the decrease of pulse-to-pulse and hatch distances led to surface morphologies that were less reflective except the increase for the red light. A local maximum reflection was obtained for wavelengths in the range from 500 to 520nm (Figures 4d-e). Wider coverage with LIPSS (σ=δ=5μm) resulted in a constant reflection of ~8% for wavelengths in the range from 500 to 700nm while there was a full absorption of violet-blue range (Figures 4e-f).

Broadband light scattering properties of the sub-wavelength features were investigated by employing near and far-field optical setups. For near-field measurements, the sample was normally illuminated and the scattered light was captured through a hemispherical surface (4cm diameter). For far-field measurements, the sample was illuminated through an angular setup [55]. Far-field diffraction patterns were captured through an image-screen setup. The two-dimensional fast Fourier transforms (2D-FFT) in Figures 3h-j were indicative of hexagonal-shaped far field

diffraction patterns. Similar 2D-FFT and diffraction patterns were previously reported for hexagonal arrangements of microstructures [6,56]. In agreement with 2D-FFT of nanoholes' arrays, hexagonal scattering patterns were observed in the surrounding of the non-diffracted broadband light (zero-order) (Figure 4g). Since the diffraction angle increases with the wavelength, multiple rainbow patterns were visible covering the range from blue to red. Analogously to diffraction gratings, the diffraction distances from the center spot were larger for the red light compared with the blue one, accordingly to Bragg's law ($\lambda/\Lambda=2\sin\phi$, where λ is the considered wavelength, Λ the grating's spacing, ϕ the angle from the surface plane) [57]. The angle-resolved far-field images indicated that PN-assisted nano-fabrication enables broad-range (up to $\theta=70°$) diffraction patterns (Figure 4h). However, lower tilt angle ($\theta=10°$) illumination shows bright far-field diffraction compare with higher tilted angle illumination ($\theta=80°$), due to omnidirectional light scattering from the edge of the micro-patterns at the bigger angle ($\theta=80°$).

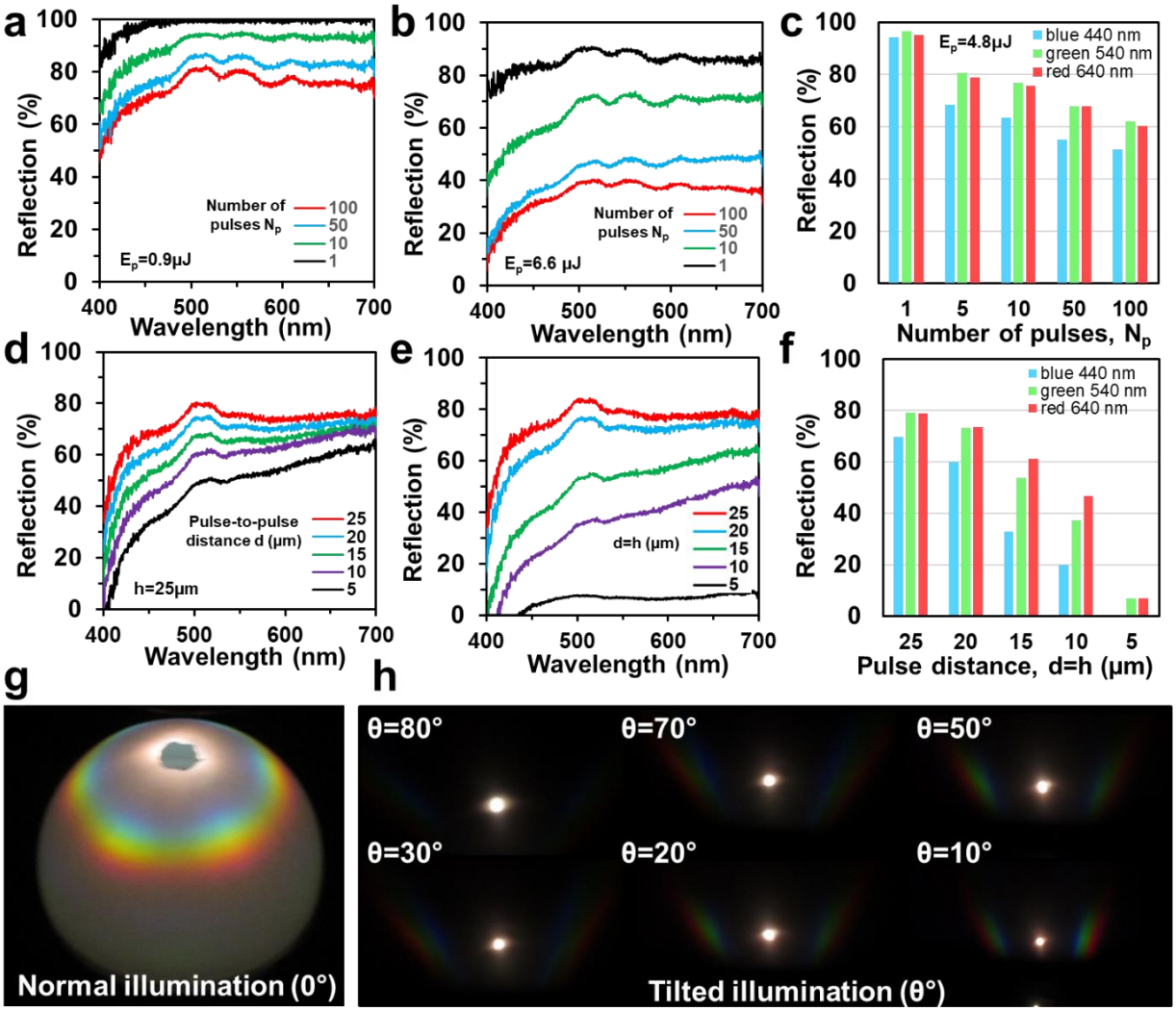

Figure 4. Optical characterization of nanotextured stainless steel. The evolution of broadband reflection with the increase of pulse numbers with two different pulse energies (a) 0.9μJ and (b) 6.6μJ. (c) The reflection evolution for three selected wavelengths, 440nm (blue), 540nm (green) and 640nm (red), with pulse numbers (constant pulse energy of 4.8μJ). The evolution of reflection properties with the pulse-to-pulse distance for (d) fixed σ=25μm and (e) σ=δ. (f) The reflection evolution for selected blue, green, red wavelengths, with the pulse-to-pulse distance σ=δ. (g) Light scattering properties under normal illumination of the surfaces, projected on a 30mm-hemispherical semi-transparent surface. (h) Light scattering properties under different illumination angles, from 10 to 80°.

3.3.2 Wettability and microbiological properties

Wettability properties of nanopatterned surfaces were investigated with 6µl of water (n=3) after prior surface cleaning, with sonication in ethanol solution and air flow drying. While non-textured stainless steel had a static water contact angle (CA) around 90° (between hydrophobic and hydrophilic), nanotexturing had two opposite effects on wetting depending on the pulse-to-pulse distance used during laser processing (Figure 5a). If the process results in arrays of nanoholes, such as for σ=δ larger than 15µm, the static contact angle decreases leading to a hydrophilic surface, with CA down to 59°. If the process results in LIPSS the CA values increased, the surface became apparently hydrophobic, with CA of 101°. In addition to the static CA, dynamic contact angle measurements were conducted for σ=δ equal to 5µm. Although LIPSS seemed to be hydrophobic (increased static and advancing contact angle), the receding contact angle remained close to the reference receding CA (Figure 5b), which leads to sticking droplets on the surface due to the high CA hysteresis (Figure 5c).

In microbial experiments, samples with a structural transition from nanoholes towards LIPSS were compared regarding their bioadhesion properties. The experiments were performed with a lab strain of E. coli (W 3110) by incubation for 4h in nutrition rich media. Instead of the originally nanostructured stainless steel samples, identical polymeric replicas were prepared for the bacterial assays, which allowed us to keep the original surface clean and available for further studies. It was shown recently that structural periodicities close to the cells size, similar to the 1 µm period of the PN-structures, support bacterial surface colonization and are, therefore, detrimental to the

inhibition of bioadhesion [8]. However, many nanotextured samples did not show an increased amount of initially adhered bacterial cells compared to the non-textured reference (Figures 5d-f). One sample type even exhibited a significantly lower bacterial colonization after 4h compared to unstructured surfaces (Figure 5e). In particular, this sample type processed at σ=δ equal to 10µm represents a transition from the hexagonally ordered nanoholes fabricated with larger pulse-to-pulse distances and self-organized subwavelength structures (LIPSS) fabricated with lower pulse-to-pulse distances (Figures 3c-g). While the bacterial assays did not show a similar monotonous trend as the static wetting measurements, interestingly, a strong increase in bacterial adhesion could be observed for the ripples-like LIPSS. SEM images in Figure 5f show that transition is accompanied by a smoothening of the surface, but periodic surface features are still visible, whereas the roughness on the LIPSS structure seems to be more pronounced.

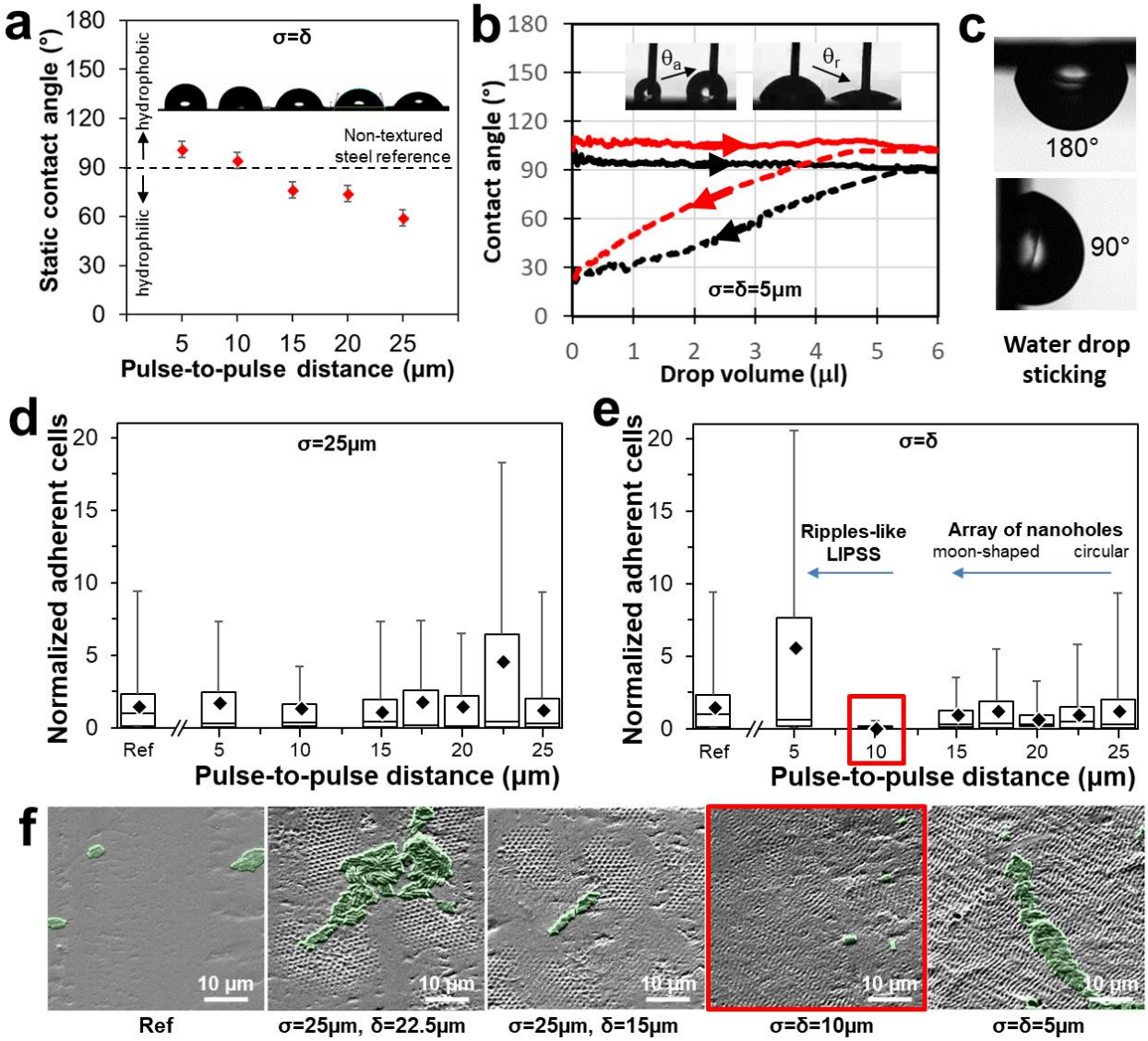

Figure 5. Wettability and microbiological characterizations of subwalength surface structures. (a) The evolution of static water CA with the pulse-to-pulse distance (σ=δ) on stainless steel. (b) Advancing and receding water CA for polished and σ=δ=5μm textured stainless steel. (c) A tilting test illustrating the sticking effect of water drops onto the σ=δ=5μm textured stainless steel. (d) The evolution of normalized adherent E. coli cells after 4h incubation on PFPE replicas with the fabricated pulse-to-pulse distance, for (d) σ=25μm and (e) σ=δ. Data are shown in box-whisker plots with half of all data points within the box and 100% within the whiskers; black diamonds in the boxes indicate mean values and the black horizontal line the median value (n=14). (f) Representative SEM images of adhered E. coli on replica of (from left to right): non-structured reference, σ=25μm and δ=22.5μm, σ=25μm and δ=15μm, σ=δ=10μm, σ=δ=5μm. The adhered E. coli cells are highlighted in green halos.

4. CONCLUSION

Microsphere-assisted nanopatterning was performed with a femtosecond near-infrared laser. A hexagonal close-packed monolayer of 1-μm-diameter silica spheres was deposited onto stainless steel and then used to generate dense arrays of PN with spot sizes smaller than the beam wavelength. The simulation results were used to estimate the near-field enhancements obtainable with microsphere sizes close to the irradiation wavelength. The minimum PN beam size was calculated to be ~470nm at the surface. Nanobumps, array of nanoholes and honeycomb structures were fabricated with periodicity equal to the microspheres' sizes. Nanoholes' arrays with 1μm spacing and a minimum diameter of 120nm were generated by employing a single pulse irradiation. Thermal side effects associated with the femtosecond pulsed PN were observable for high fluences with detrimental impact on nanoholes' homogeneity. A beam focal offset was beneficial for the single-pulse fabrication of homogeneous nanoholes, however microspheres were removed from the immediate vicinity of textured areas. Multiple pulses could not improve the typically 1:10 aspect ratio but led to a range of surface self-organized structures (LIPSS). Interestingly, the fluence threshold for LIPSS generation was reduced and the LIPSS periodicity could be tailored according to the microspheres' sizes. The nanoholes' filling ratio could be optimized by employing pulse-to-pulse distances and thus to minimize the DLC effect in single-pulse processing. LIPSS could also be generated to close gaps between islands of nanoholes' array. Multiple characterization of surface functionalities were performed for different arrays of

nanoholes and LIPSS. Surfaces exhibited efficient broad range light scattering (up to θ=70°). Surface reflection and scattering properties could be tailored and specific visible wavelength range could be absorbed. The wetting of the textured surfaces responded differently for array of holes than for LIPSS, showing a monotonous decrease of the static contact angle from 100° for LIPSS down to 60° for hexagonal-arranged nanoholes, correlating with the gradually change of process parameters. No similar comprehensive trend could be found in microbial adhesion tests, but there was a significant decrease in bacterial surface colonization after 4h on surfaces situated in the transition between nanohole and LIPSS structures. This could open a new pathway for future studies to evaluate the PN-assisted technology for inhibition of bacterial adhesion.

ACKNOWLEDGMENT

The authors would like to acknowledge Tarek Alashraf at Leibniz-IPF, in processing micrographs for counting the attached bacteria.

FUNDING

This work was carried out within the framework of the H2020 ITN programme "European ESRs Network on Short Pulsed Laser Micro/Nanostructuring of Surfaces for Improved Functional Applications" under the Marie Skłodowska-Curie grant agreement No. 675063 (www.laser4fun.eu). In addition, the work was supported by two other H2020 FoF programmes, i.e. the projects on "Modular laser based additive manufacturing platform for large scale industrial applications" (MAESTRO) and "High-Impact Injection Moulding Platform for mass-production of 3D and/or large micro-structured surfaces with Antimicrobial, Self-cleaning, Anti-scratch, Anti-squeak and Aesthetic functionalities" (HIMALAIA).

REFERENCES

[1] E. Skoulas, A. Manousaki, C. Fotakis, E. Stratakis, Biomimetic surface structuring using cylindrical vector femtosecond laser beams, Sci. Rep. 7 (2017) srep45114. doi:10.1038/srep45114.

[2] I. Gnilitskyi, L. Orazi, N.M. Bulgakova, T.J.-Y. Derrien, T. Mocek, Y. Levy, High-speed manufacturing of highly regular femtosecond laser-induced periodic surface structures: physical origin of regularity, Sci. Rep. 7 (2017) 8485. doi:10.1038/s41598-017-08788-z.

[3] L. Müller-Meskamp, Y.H. Kim, T. Roch, S. Hofmann, R. Scholz, S. Eckardt, K. Leo, A.F. Lasagni, Efficiency Enhancement of Organic Solar Cells by Fabricating Periodic Surface Textures using Direct Laser Interference Patterning, Adv. Mater. 24 (2012) 906–910. doi:10.1002/adma.201104331.

[4] H. Palneedi, J.H. Park, D. Maurya, M. Peddigari, G.-T. Hwang, V. Annapureddy, J.-W. Kim, J.-J. Choi, B.-D. Hahn, S. Priya, K.J. Lee, J. Ryu, Laser Irradiation of Metal Oxide Films and Nanostructures: Applications and Advances, Adv. Mater. 30 (2018). doi:10.1002/adma.201705148.

[5] D. Huerta-Murillo, A. García-Girón, J.M. Romano, J.T. Cardoso, F. Cordovilla, M. Walker, S.S. Dimov, J.L. Ocaña, Wettability modification of laser-fabricated hierarchical surface structures in Ti-6Al-4V titanium alloy, Appl. Surf. Sci. 463 (2019) 838–846. doi:10.1016/j.apsusc.2018.09.012.

[6] J.-M. Romano, A. Garcia-Giron, P. Penchev, S. Dimov, Triangular laser-induced submicron textures for functionalising stainless steel surfaces, Appl. Surf. Sci. 440C (2018) 162–169.

[7] K.A. Whitehead, J. Colligon, J. Verran, Retention of microbial cells in substratum surface features of micrometer and sub-micrometer dimensions, Colloids Surf. B Biointerfaces. 41 (2005) 129–138. doi:10.1016/j.colsurfb.2004.11.010.

[8] R. Helbig, D. Günther, J. Friedrichs, F. Rößler, A. Lasagni, C. Werner, The impact of structure dimensions on initial bacterial adhesion, Biomater Sci. 4 (2016) 1074–1078. doi:10.1039/C6BM00078A.

[9] K. Anselme, P. Davidson, A.M. Popa, M. Giazzon, M. Liley, L. Ploux, The interaction of cells and bacteria with surfaces structured at the nanometre scale, Acta Biomater. 6 (2010) 3824–3846. doi:10.1016/j.actbio.2010.04.001.

[10] G. Yi, Y. Yuan, X. Li, Y. Zhang, ZnO Nanopillar Coated Surfaces with Substrate-Dependent Superbactericidal Property, Small. 14 (2018) 1703159. doi:10.1002/smll.201703159.

[11] A. Cunha, A.-M. Elie, L. Plawinski, A.P. Serro, A.M. Botelho do Rego, A. Almeida, M.C. Urdaci, M.-C. Durrieu, R. Vilar, Femtosecond laser surface texturing of titanium as a method to reduce the adhesion of Staphylococcus aureus and biofilm formation, Appl. Surf. Sci. 360, Part B (2016) 485–493. doi:10.1016/j.apsusc.2015.10.102.

[12] M. Bieda, M. Siebold, A.F. Lasagni, Fabrication of sub-micron surface structures on copper, stainless steel and titanium using picosecond laser interference patterning, Appl. Surf. Sci. 387 (2016) 175–182. doi:10.1016/j.apsusc.2016.06.100.

[13] R. Ahmed, A.K. Yetisen, A.E. Khoury, H. Butt, Printable ink lenses, diffusers, and 2D gratings, Nanoscale. 9 (2017) 266–276. doi:10.1039/C6NR07841A.

[14] J.F. Young, J.S. Preston, H.M. van Driel, J.E. Sipe, Laser-induced periodic surface structure. II. Experiments on Ge, Si, Al, and brass, Phys. Rev. B. 27 (1983) 1155–1172. doi:10.1103/PhysRevB.27.1155.
[15] A. Heifetz, S.-C. Kong, A.V. Sahakian, A. Taflove, V. Backman, Photonic Nanojets, J. Comput. Theor. Nanosci. 6 (2009) 1979–1992. doi:10.1166/jctn.2009.1254.
[16] S.-M. Yang, S.G. Jang, D.-G. Choi, S. Kim, H.K. Yu, Nanomachining by Colloidal Lithography, Small. 2 (2006) 458–475. doi:10.1002/smll.200500390.
[17] E. Abbe, Beiträge zur Theorie des Mikroskops und der mikroskopischen Wahrnehmung, Arch. Für Mikrosk. Anat. 9 (1873). http://publikationen.ub.uni-frankfurt.de/frontdoor/index/index/docId/11525 (accessed February 28, 2018).
[18] Z. Chen, A. Taflove, V. Backman, Photonic nanojet enhancement of backscattering of light by nanoparticles: a potential novel visible-light ultramicroscopy technique, Opt. Express. 12 (2004) 1214–1220.
[19] S. Lecler, Y. Takakura, P. Meyrueis, Properties of a three-dimensional photonic jet, Opt. Lett. 30 (2005) 2641–2643. doi:10.1364/OL.30.002641.
[20] O. Delléa, O. Shavdina, P. Fugier, P. Coronel, E. Ollier, S.-F. Désage, Control Methods in Microspheres Precision Assembly for Colloidal Lithography, in: Precis. Assem. Technol. Syst., Springer, Berlin, Heidelberg, 2014: pp. 107–117. doi:10.1007/978-3-662-45586-9_14.
[21] S.M. Huang, M.H. Hong, B.S. Luk'yanchuk, Y.W. Zheng, W.D. Song, Y.F. Lu, T.C. Chong, Pulsed laser-assisted surface structuring with optical near-field enhanced effects, J. Appl. Phys. 92 (2002) 2495–2500. doi:10.1063/1.1501768.
[22] E. McLeod, C.B. Arnold, Subwavelength direct-write nanopatterning using optically trapped microspheres, Nat. Nanotechnol. 3 (2008) 413–417. doi:10.1038/nnano.2008.150.
[23] S. Theppakuttai, S. Chen, Nanoscale surface modification of glass using a 1064 nm pulsed laser, Appl. Phys. Lett. 83 (2003) 758–760. doi:10.1063/1.1597425.
[24] A. Abdurrochman, S. Lecler, F. Mermet, B.Y. Tumbelaka, B. Serio, J. Fontaine, Photonic jet breakthrough for direct laser microetching using nanosecond near-infrared laser, Appl. Opt. 53 (2014) 7202–7207. doi:10.1364/AO.53.007202.
[25] W. Guo, Z.B. Wang, L. Li, Z. Liu, B. Luk'yanchuk, D.J. Whitehead, Chemical-assisted laser parallel nanostructuring of silicon in optical near fields, Nanotechnology. 19 (2008) 455302. doi:10.1088/0957-4484/19/45/455302.
[26] D. McCloskey, Y.P. Rakovich, J.F. Donegan, Controlling the properties of Photonic Jets, in: 2010 12th Int. Conf. Transparent Opt. Netw., 2010: pp. 1–3. doi:10.1109/ICTON.2010.5548948.
[27] L. Han, Y. Han, G. Gouesbet, J. Wang, G. Gréhan, Photonic jet generated by spheroidal particle with Gaussian-beam illumination, JOSA B. 31 (2014) 1476–1483. doi:10.1364/JOSAB.31.001476.
[28] D. Grojo, N. Sandeau, L. Boarino, C. Constantinescu, N.D. Leo, M. Laus, K. Sparnacci, Bessel-like photonic nanojets from core-shell sub-wavelength spheres, Opt. Lett. 39 (2014) 3989–3992. doi:10.1364/OL.39.003989.
[29] Y.W. Zheng, B.S. Luk'yanchuk, Y.F. Lu, W.D. Song, Z.H. Mai, Dry laser cleaning of particles from solid substrates: Experiments and theory, J. Appl. Phys. 90 (2001) 2135–2142. doi:10.1063/1.1389477.

[30] N. Arnold, Theoretical description of dry laser cleaning, Appl. Surf. Sci. 208–209 (2003) 15–22. doi:10.1016/S0169-4332(02)01278-3.
[31] M. Mosbacher, V. Dobler, J. Boneberg, P. Leiderer, Universal threshold for the steam laser cleaning of submicron spherical particles from silicon, Appl. Phys. A. 70 (2000) 669–672. doi:10.1007/PL00021079.
[32] G. Vereecke, E. Röhr, M.M. Heyns, Laser-assisted removal of particles on silicon wafers, J. Appl. Phys. 85 (1999) 3837–3843. doi:10.1063/1.369754.
[33] C. O'Connell, R.J. Sherlock, T.J. Glynn, Fabrication of a reusable microlens array for laser-based structuring, Opt. Eng. 49 (2010) 014201. doi:10.1117/1.3281665.
[34] A. Khan, Z. Wang, M.A. Sheikh, D.J. Whitehead, L. Li, Parallel near-field optical micro/nanopatterning on curved surfaces by transported micro-particle lens arrays, J. Phys. Appl. Phys. 43 (2010) 305302. doi:10.1088/0022-3727/43/30/305302.
[35] A. Khan, Z. Wang, M.A. Sheikh, D.J. Whitehead, L. Li, Laser micro/nano patterning of hydrophobic surface by contact particle lens array, Appl. Surf. Sci. 258 (2011) 774–779. doi:10.1016/j.apsusc.2011.08.089.
[36] X. Sedao, T.J.-Y. Derrien, G.R.B.E. Romer, B. Pathiraj, A.J. Huis in 't Veld, Laser surface micro-/nano-structuring by a simple transportable micro-sphere lens array, J. Appl. Phys. 112 (2012) 103111. doi:10.1063/1.4767471.
[37] Z. Tebby, O. Dellea, Method for Depositing a Layer of Organized Particles on a Substrate, WO2011107681 (A1), 2011. https://worldwide.espacenet.com/publicationDetails/biblio?FT=D&date=20110909&DB=EPODOC&locale=&CC=WO&NR=2011107681A1&KC=A1&ND=4 (accessed February 28, 2018).
[38] A. Pereira, D. Grojo, M. Chaker, P. Delaporte, D. Guay, M. Sentis, Laser-Fabricated Porous Alumina Membranes for the Preparation of Metal Nanodot Arrays, Small. 4 (2008) 572–576. doi:10.1002/smll.200700256.
[39] K.-H. Leitz, U. Quentin, B. Hornung, A. Otto, I. Alexeev, M. Schmidt, Microsphere near-field nanostructuring using picosecond pulses, Phys. Procedia. 5 (2010) 237–244. doi:10.1016/j.phpro.2010.08.142.
[40] H.-J. Münzer, M. Mosbacher, M. Bertsch, J. Zimmermann, P. Leiderer, J. Boneberg, Local field enhancement effects for nanostructuring of surfaces, J. Microsc. 202 (2001) 129–135. doi:10.1046/j.1365-2818.2001.00876.x.
[41] W. Cai, R. Piestun, Patterning of silica microsphere monolayers with focused femtosecond laser pulses, Appl. Phys. Lett. 88 (2006) 111112. doi:10.1063/1.2183733.
[42] S. Li, Z. Yang, Z. Zhang, F. Gao, J. Du, S. Zhang, Study of nanospheres lithography technology with super-lens for fabricating nano holes, J. Appl. Phys. 113 (2013) 183102. doi:10.1063/1.4803845.
[43] Refractive index of SiO2, (n.d.). https://refractiveindex.info/?shelf=main&book=SiO2&page=Radhakrishnan-o (accessed June 28, 2018).
[44] A.V. Itagi, W.A. Challener, Optics of photonic nanojets, JOSA A. 22 (2005) 2847–2858. doi:10.1364/JOSAA.22.002847.
[45] M. Mosbacher, H.-J. Münzer, J. Zimmermann, J. Solis, J. Boneberg, P. Leiderer, Optical field enhancement effects in laser-assisted particle removal, Appl. Phys. A. 72 (2001) 41–44. doi:10.1007/s003390000715.

[46] K. Piglmayer, R. Denk, D. Bäuerle, Laser-induced surface patterning by means of microspheres, Appl. Phys. Lett. 80 (2002) 4693–4695. doi:10.1063/1.1489085.
[47] K. Vestentoft, J.A. Olesen, B.H. Christensen, P. Balling, Nanostructuring of surfaces by ultra-short laser pulses, Appl. Phys. A. 80 (2005) 493–496. doi:10.1007/s00339-004-3079-y.
[48] W. Guo, Z.B. Wang, L. Li, D.J. Whitehead, B.S. Luk'yanchuk, Z. Liu, Near-field laser parallel nanofabrication of arbitrary-shaped patterns, Appl. Phys. Lett. 90 (2007) 243101. doi:10.1063/1.2748035.
[49] L. Li, W. Guo, Z.B. Wang, Z. Liu, D. Whitehead, B. Luk'yanchuk, Large-area laser nano-texturing with user-defined patterns, J. Micromechanics Microengineering. 19 (2009) 054002. doi:10.1088/0960-1317/19/5/054002.
[50] S.M. Huang, Z. Sun, B.S. Luk'yanchuk, M.H. Hong, L.P. Shi, Nanobump arrays fabricated by laser irradiation of polystyrene particle layers on silicon, Appl. Phys. Lett. 86 (2005) 161911. doi:10.1063/1.1886896.
[51] Y. Zhou, M.H. Hong, J. Fuh, L. Lu, B.S. Luk'yanchuk, Z.B. Wang, L.P. Shi, T.C. Chong, Direct femtosecond laser nanopatterning of glass substrate by particle-assisted near-field enhancement, Appl. Phys. Lett. 88 (2006) 023110. doi:10.1063/1.2163988.
[52] N.N. Nedyalkov, P.A. Atanasov, M. Obara, Near-field properties of a gold nanoparticle array on different substrates excited by a femtosecond laser, Nanotechnology. 18 (2007) 305703.
[53] D. Grojo, A. Cros, P. Delaporte, M. Sentis, Time-of-flight measurements of ejected particles during dry laser cleaning, Appl. Phys. B. 84 (2006) 517–521. doi:10.1007/s00340-006-2283-1.
[54] L.N.D. Kallepalli, D. Grojo, L. Charmasson, P. Delaporte, O. Utéza, A. Merlen, A. Sangar, P. Torchio, Long range nanostructuring of silicon surfaces by photonic nanojets from microsphere Langmuir films, J. Phys. Appl. Phys. 46 (2013) 145102. doi:10.1088/0022-3727/46/14/145102.
[55] R. Ahmed, A.K. Yetisen, S.H. Yun, H. Butt, Color-selective holographic retroreflector array for sensing applications, Light Sci. Appl. 6 (2017) e16214. doi:10.1038/lsa.2016.214.
[56] R. Ahmed, A.K. Yetisen, H. Butt, High Numerical Aperture Hexagonal Stacked Ring-Based Bidirectional Flexible Polymer Microlens Array, ACS Nano. 11 (2017) 3155–3165. doi:10.1021/acsnano.7b00211.
[57] R. Ahmed, A.A. Rifat, M.U. Hassan, A.K. Yetisen, H. Butt, Phase-conjugated directional diffraction from a retroreflector array hologram, RSC Adv. 7 (2017) 25657–25664. doi:10.1039/C7RA04131D.